Materials Today Bio 32 (2025) 101761

Contents lists available at ScienceDirect

Materials Today Bio

journal homepage: www.journals.elsevier.com/materials-today-bio

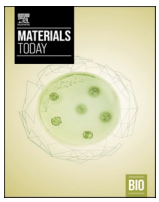

Dual-responsive nanoscale ultrasound contrast agent as an oxidative stress amplifier for enhanced DNA damage in BRCA-proficient ovarian cancer

Jialu Zhang [a,1], Xiaoxuan Wang [a,1], Lu Guo [a], Shan Xiao [a], Dong Meng [a], Mengmeng Shang [a], Xiao Sun [a], Dandan Shi [a], Yading Zhao [a], Rui Liu [a], Shuting Huang [a], Xinyu Zeng [a], Jie Li [a,b,*]

[a] Department of Ultrasound, Qilu Hospital of Shandong University, Jinan, Shandong, 250012, China
[b] Department of Ultrasound, Qilu Hospital (Qingdao) of Shandong University, Qingdao, Shandong, 266035, China

ARTICLE INFO

Keywords:
Ovarian cancer
Ultrasound-targeted microbubble destruction
DNA damage
Reactive oxygen species
Mitochondrial dysfunction

ABSTRACT

PARP inhibitor (PARPi)-based synthetic lethal therapies have displayed limited benefits in BRCA-proficient ovarian cancer. To potentiate the application of PARPi, an ultrasound contrast agent OLA-NDs for delivery of the PARPi olaparib (OLA) was established for enhancing DNA damage by blocking DNA repair. OLA-NDs were endowed with endogenous pH- and exogenous ultrasound (US)-responsiveness to target tumors, as well as contrast-enhanced US imaging for diagnostic and therapeutic integration. OLA-NDs could upregulate NOX4 to induce oxidative stress and sensitize BRCA wild-type A2780 cells to DNA oxidative damage through the utilization of ultrasound-targeted microbubble destruction (UTMD). In addition, the strategy further increased ROS production by interfering with mitochondrial function, thereby exacerbating DNA double-strand breaks (DSBs) and inducing mitochondria-mediated apoptosis. As a consequence, the combined application of UTMD and OLA-NDs demonstrated significant antitumor effects *in vitro* and *in vivo*. This combined strategy of amplifying oxidative damage improved lethality by promoting DNA DSBs and apoptosis with reduced adverse side effects, which would provide new insight for the clinical application of PARPi in BRCA-proficient ovarian cancer.

1. Introduction

Ovarian cancer consists of multiple histological types, 90 % of ovarian cancers are of an epithelial cell type, and is the malignant tumor of the female reproductive system with the highest mortality rate in the world [1]. The remaining 10 % are non-epidermal ovarian cancer with a good prognosis, such as germ cell tumors and sex cord-stromal tumors [2]. Although CA125 has been FDA-approved for monitoring in epithelial ovarian cancer, and its integration with HE4 in clinical decision algorithms (e.g., ROMA) represents ongoing improvements in early detection strategies, the diagnostic sensitivity remains suboptimal [3]. The combination of these tools aims to improve early detection, though limitations persist in sensitivity for early-stage disease. As a result, approximately 70 % of patients have progressed to advanced disease at the time of first diagnosis [4]. Although most patients initially respond well to standard first-line therapy, recurrences have been reported frequently, with five-year survival rates below 40 % [5]. Therefore, it is crucial to optimize first-line treatment strategies to improve ovarian cancer cure rates [6].

With the success of targeted therapies, new biological agents such as PI3K inhibitors and Poly (ADP-ribose) polymerase inhibitors (PARPi) have emerged in recent clinical trials, which play an important role in cancer cell survival by regulating DNA replication and cell cycle [7]. PARPi are designed to inhibit PARP activity to prevent DNA single-strand breaks (SSBs) repair and trap PARPs on DNA to interfere with DNA replication, consequently leading to the formation of DNA double-strand breaks (DSBs) and cell death [,8–10]. In BRCA-mutant tumors, PARPi has established promising antitumor activity through synthetic lethal due to homologous recombination (HR) deficiency, making PARPi more sensitive to BRCA-mutant tumors than BRCA-proficient tumors [11,12]. Recent studies have shown that PARPi could activate innate immune cGAS-STING signaling to control BRCA-proficient tumors in the immune microenvironment and can be used as a maintenance therapy for BRCA-proficient tumors [13,14]. This brought new perspectives for the application of PARPi in BRCA-proficient tumors, but hematological toxicity and tumor

* Corresponding author. Department of Ultrasound, Qilu Hospital of Shandong University, Jinan, Shandong, 250012, China.
E-mail address: jieli@email.sdu.edu.cn (J. Li).
[1] Jialu Zhang and Xiaoxuan Wang contributed equally to this work.

https://doi.org/10.1016/j.mtbio.2025.101761
Received 16 January 2025; Received in revised form 6 April 2025; Accepted 10 April 2025
Available online 11 April 2025

resistance of PARPi also became inevitable [15,16]. Compared with monotherapy, combination therapy has three major advantages, including: improving anticancer efficacy, expanding drug use scenarios, and delaying drug resistance. Thus, it is urgent to develop novel synergistic strategies for expanding the safe application of PARPi in BRCA-proficient ovarian cancer.

Drug delivery systems (DDSs) have appeared as a powerful tool for free drugs to increase bioavailability and minimize side effects. However, due to the presence of a high-density extracellular matrix, poor penetration remains an obstacle to DDSs-mediated cancer therapy [17]. Owing to its controllable, noninvasive, and highly tissue penetrability, US has been widely applied not only in clinical diagnosis but also in cancer therapy [18]. Ultrasound-targeted microbubble destruction (UTMD) is an US-mediated therapeutic technology that utilizes the reaction of ultrasound contrast agents (UCAs) with mechanical forces to increase tissue and cell membrane permeability for site-specific drug delivery [19–21]. In addition, UTMD could lead to increased intracellular reactive oxygen species (ROS) [22,23]. Physiological levels of ROS could transmit intracellular signals, while an imbalance between ROS generation and cellular defenses will result in cells under oxidative stress, which triggers oxidative damage to biomolecules including proteins and DNA [24–27]. NADPH oxidases 4 (NOX4), a member of the NOX family of enzymes, controls various cellular processes through the production of ROS, and recent studies have shown that NOX4 is involved in the regulation of drug resistance and tumor metabolic processes [28,29]. Therefore, UTMD may enhance DNA damage by upregulating NOX4-induced oxidative stress, which increases the killing effect on cancer cells. Sustained DNA damage may activate DNA repair mechanisms, which would prevent tumor apoptosis and lead to a significantly reduced therapeutic outcome [30–32]. Perhaps it is feasible to construct UCAs to inhibit DNA damage repair and amplify oxidative damage from UTMD.

Herein, we present a new strategy that combines UTMD and PARPi for amplifying DNA damage in cancer. In this work, we designed a nanoscale UCA delivering the classical PARPi olaparib (OLA), named OLA-NDs. O-carboxymethyl chitosan (O-CMC), which serves as the shell of the OLA-NDs, is a biodegradable polysaccharide that accumulates and releases encapsulated drugs in the acidic tumor microenvironment (TME). The core of OLA-NDs is perfluorohexane (PFH), which facilitates drug release and penetration deep into tumor tissue via US-stimulated acoustic droplet vaporization (ADV) and could be used for contrast-enhanced ultrasound (CEUS) imaging. Benefiting from the pH- and US-responsiveness of OLA-NDs in tumors, OLA would be rapidly released, inhibiting DNA repair and sensitizing cancer cells to ROS-mediated oxidative damage. Meanwhile, UTMD triggers generate robust ROS that induce DNA damage and oxidative stress for cancer cell killing. Ultimately, the combination therapy reduces adverse effects while suppressing tumors (Fig. 1). This strategy of amplifying oxidative damage based on UCAs sheds light on the application of PARPi in BRCA-proficient ovarian cancer.

2. Materials and methods

2.1. Materials

O-CMC and N-Acetylcysteine (NAC) were supplied by Macklin (Shanghai, China). Tween 20, CCK-8 and JC-1 were provided by Solarbio (Beijing, China). OLA and PFH (C_6F_{14}) were supplied by Aladdin (Shanghai, China). Comet assay kit was acquired from Abbkine (Wuhan, China). Viability/Cytotoxicity assay kit and DCFH-DA were provided by Beyotime (Shanghai, China). Anti-BAX, anti-Bcl-2, anti-γ-H2AX antibodies were supplied by Abcam (Cambridge, UK). Anti-NOX-4 and anti-β-actin antibodies were acquired from Proteintech (Wuhan, China). Anti-8-OHdG were provided by Santa Cruz (TX, USA).

2.2. Cell culture and animal model

A2780 (human ovarian cancer) cells were supplied by ATCC and cultured in DMEM containing 10 % FBS. OLA concentration was 40 μg/mL, US parameters were 0.5 W cm^{-2}, 60 s. NAC (10 mM) was used in

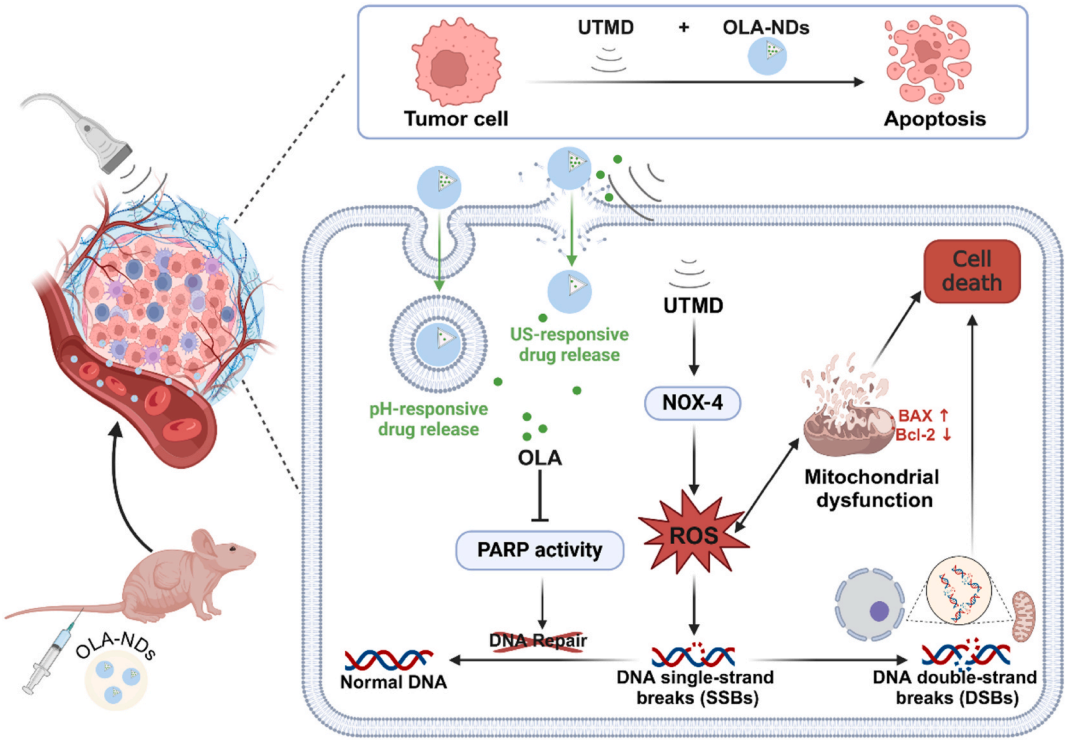

Fig. 1. Illustration of the combination of UTMD with OLA-NDs inducing oxidative stress for enhanced DNA damage in tumor cell. The figure is created with BioRender.com.

some experiments to pretreat cells.

Female BALB/c nude mice (4–5 weeks) were purchased from Vital River Company (Beijing, China). A2780 cells suspension (5×10^6 cells) was injected into the right flank of each mouse subcutaneously. OLA dose for 50 mg/kg per mouse, US parameters were 1.25 W cm^{-2}, 1 min.

2.3. Preparation of (OLA-)NDs

The mixture of lecithin, Tween 20 and PFH was processed in an ultrasonic crusher (UP250, Scientz, China) for 5 min at 150 W in ice bath. Then, re-sonication was performed by dropwise addition of O-CMC solution with or without OLA. Suspensions were centrifuged at low speed for 5 min to obtain the intermediate layer, which was then centrifuged for 15 min at 13,000 rpm. Precipitates were washed with PBS in order to remove impurities and free drug.

2.4. Characterization of (OLA-)NDs

Morphology of OLA-NDs was examined by transmission electron microscopy (TEM, Tokyo, Japan). The particle size, polydispersity index (PDI), and ζ potential of OLA-NDs at different pH values (pH 7.4, pH 6.5, and pH 5.5) were analyzed by Dynamic light scattering (DLS, Malvern Zetasizer Nano, UK). Besides, ζ potential were assessed in pH 7.4, pH 7.1, pH 6.8, and pH 5.5. The particle size and PDI were also evaluated within 48 h in 10 % FBS and under lyophilization.

The loading efficiency (LE) and encapsulation efficiency (EE) of OLA in OLA-NDs were determined by UV spectrophotometer (DeNovix, Wilmington, USA). After the optimal encapsulation efficiency of fresh nanodrops was detected, it was compared with the encapsulation efficiency of nanodrops obtained after lyophilization. To assess the pH responsiveness, OLA-NDs solutions were loaded into dialysis bag and placed in PBS of different pH as mentioned above at 100 rpm. At the set time, removed 1 mL aliquot and added 1 mL of fresh PBS. To assess the US responsiveness, OLA-NDs solution in the dialysis bag was subjected to US irradiation and treated as described above. In addition, the drug release behavior after US exposure was studied under different pH conditions. After incubation of OLA-NDs with PBS at different pH for 4 h, the respective supernatants were collected, detected, and removed, considered the drug loading at this time as 100 %. Then ultrasonic stimulation was applied and the supernatant was collected at different time intervals. The accumulative release of OLA was calculated by UV spectrophotometer.

To determine whether a phase transition occurred at 37 °C, a test tube containing the OLA-NDs sample was immersed in a water bath and then dropped onto a slide and observed under microscope. To demonstrate the ADV, NDs were added to the well plates for US irradiated, and then dropped on slides and observed under microscope. Besides, the particle sizes of NDs with or without US were subsequently tested by DLS.

Hemolysis assay was used to examine the hemocompatibility of NDs. NDs were added to mouse blood cells and incubated 1 h at 37 °C. Optical density (OD) of the supernatant was assessed using microplate reader (Infinite M200, TECAN, Switzerland) at 545 nm.

2.5. CEUS imaging

An US diagnostic instrument with a 9 L linear transducer (LOGIQ E9, GE, USA) was used for US imaging. For *in vitro*, PBS or OLA-NDs solution was injected into latex gloves that were immersed in water for imaging. Tumor-bearing mice were anesthetized and the tumor was imaged after intravenous injection with 200 μL of PBS or OLA-NDs for *in vivo* imaging.

2.6. Tumor-targeting ability

Cellular uptake of NDs was observed through confocal laser scanning microscope (CLSM, Olympus SpinSR10, Japan). A2780 cells were incubated with Dil-labeled NDs, US irradiated after 0.5 h. Cells were incubated in dishes of different pH for 2 h for the pH response, finally observed by CLSM. Besides, the cellular uptake of OLA-NDs was investigated on LX2 cells.

Tumor-bearing mice were anesthetized and injected intravenously with Dil-labeled NDs, the fluorescence signal was visualized and quantified at set times with the IVIS imaging system. Mice were executed at 24 h, tumors were dissected for fixed and dehydrated, then sectioned and stained with DAPI, and visualized with CLSM.

2.7. Intracellular ROS measurement

A2780 cells were planted in 6-well plants for 24 h after different treatments. ROS production in A2780 cells was labeled with the fluorescent probe DCFH-DA and observed with fluorescence microscope.

2.8. Alkaline comet assay

Cell suspension was fixed and embodied in agarose which above in comet slides. Then, the cells were lysed and electrophoresed with alkaline electrophoresis solution at 20 V/300 mA. Cells were stained with propidium iodide (PI) and observed by fluorescence microscopy. Comet tail length and percentage of DNA in the tail (TailDNA%) can be used to assess the extent of DNA, with TailDNA% defined as tail DNA intensity/total DNA intensity × 100 %.

2.9. Calculation of PARP activity

PARP activity was determined by ELISA kits. Firstly, different groups of cells were lysed and centrifuged to obtain the supernatant. Then the prepared standards, samples and blank groups were added to the assay wells and the other components were added step by step according to the instructions and the absorbance was measured using a microplate reader.

2.10. Immunofluorescence

Cells were fixed and permeabilized for 24 h after different treatments, and incubated with primary antibody overnight at 4 °C. Then, cells were incubated with fluorescently labeled secondary antibody, stained with DAPI and observed by fluorescence microscopy. Immunofluorescence quantitative analysis was completed by Image J software.

2.11. Cell cycle

The cell cycle was analyzed by PI staining. After 12 h of incubation with different treatments, cells were collected, centrifuged and fixed overnight in 75 % ethanol. Cells were stained with PI, quantified by flow cytometry and analyzed using ModFit LT software.

2.12. Mitochondrial membrane potential (MMP) detection

MMP changes were detected using the fluorescent probe JC-1. After different treatments, cells were added with JC-1 staining solution and incubated for 20 min at 37 °C. Then cells were observed by fluorescence microscope.

2.13. Bio-TEM imaging

Mitochondrial morphology of different groups of cells was examined by TEM. Cells after 24 h of treatment were digested and centrifuged and resuspended with 2.5 % glutaraldehyde. After embedding, ultrathin sections were made and observed under TEM.

2.14. Western blot

Protein extracted from six groups of cells after different treatments were subjected to electrophoresis, membrane transfer, and incubation of primary and secondary antibodies. Visualization of the protein bands were done by the chemiluminescence instrument (Tanon-4800, Shanghai, China). Gray scale values were analyzed using Image J software.

2.15. In vitro antitumor ability

Viability/cytotoxicity assay kits are used to assess the live and dead of different groups on cells. A2780 cells were planted in 12-well plants for 24 h after different treatments. Cells were incubated with Calcein AM/PI working solution at 37 °C for 30 min and observed by fluorescence microscopy.

Cell proliferation was assayed by EdU kit. Cells were stained according to the instruction method at 24 h after the different treatments and observed with fluorescence microscopy.

Cell viability was assessed by CCK-8 assay. A2780 cells were cultured in 96-well plates (5×10^3 cells/well), the medium was changed with a 9:1 mixture of DMEM and CCK-8 solution at 24 h after the different treatments. Absorbance was calculated at 450 nm using microplate reader.

Cell migration was assessed by wound healing assay. A2780 cells were planted in 6-well plates, and wounds were created with a 200 μL pipette tip. Cells were cultured in DMEM containing 2 % FBS for 48 h after different treatments. Relative wound healing area (%) = (Wound area at 0 h - Wound area at 48 h)/Wound area at 0 h × 100 %. Wound area was quantified with Image J.

Cell invasion was assessed through transwell assay. Matrigel was placed in the transwell chamber and allowed to solidify, 2×10^5 cells resuspended in 200 μL DMEM without FBS at the upper layer. 600 μL DMEM containing 15 % FBS was added in the lower layer. Cells were fixed and stained after 24 h. Invasive cells were counted under microscope.

2.16. In vivo antitumor ability

When tumors reached 50 mm^3, mice were randomly divided into 6 groups (n = 5). Tumor volume and body weight were assessed every 2 days, and treatment was administered via intravenously every 3 days in

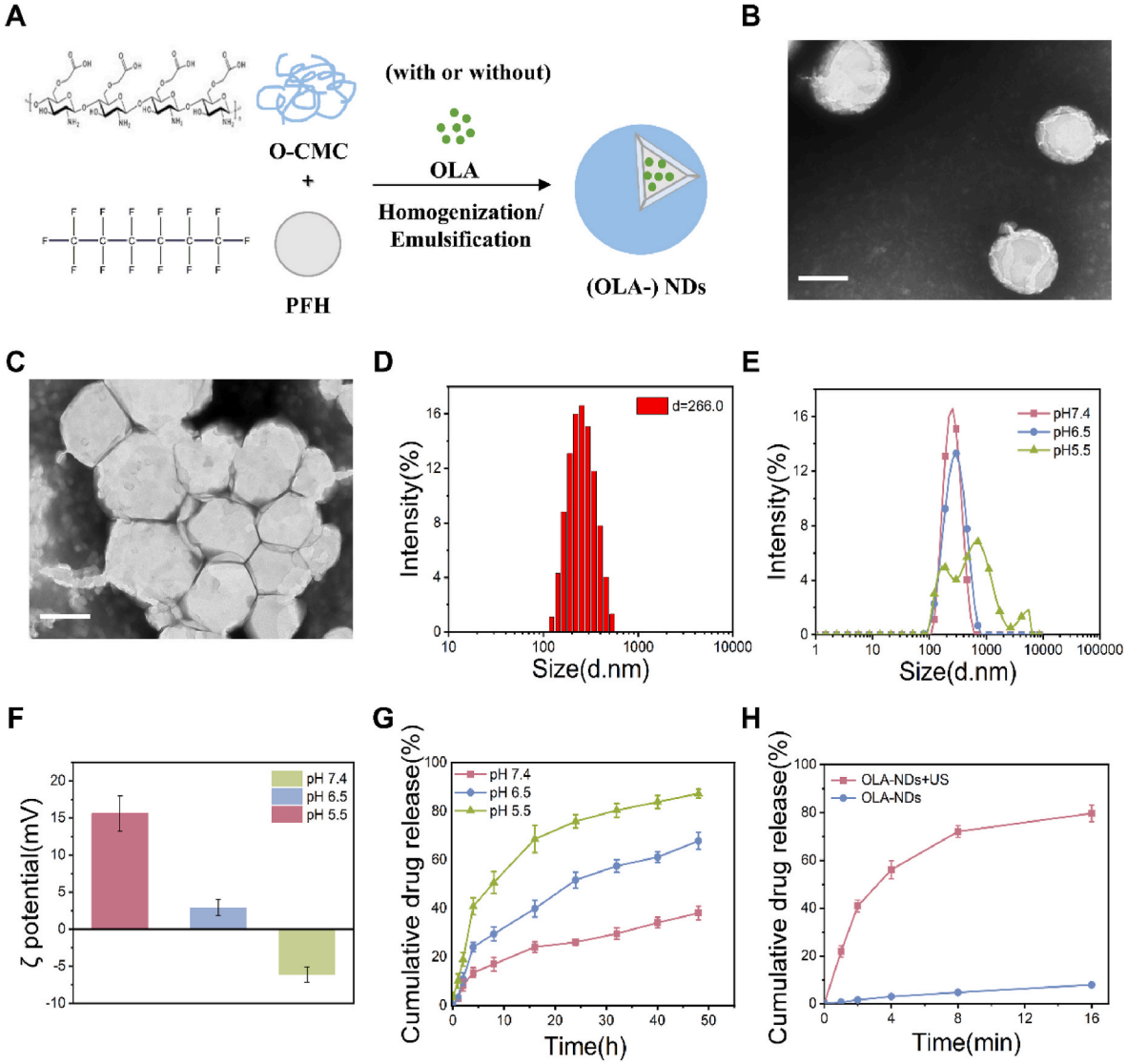

Fig. 2. Characterization of OLA-NDs. (A) Illustration of NDs and OLA-NDs. (B) TEM images of OLA-NDs at pH 7.4. Scale bar: 200 nm. (C) TEM images of OLA-NDs at pH 5.5. Scale bar: 200 nm. (D) Size distribution of OLA-NDs at pH 7.4. (E) Size distribution of OLA-ND at different pH. (F) ζ potential of OLA-NDs at different conditions. (G) Drug release behavior of OLA-NDs at different conditions. (H) Drug release behavior of OLA-NDs after US exposure.

each group. After 12 days, mice were executed and tumors were dissociated for immunofluorescence, immunohistochemistry (IHC), H&E, and TUNEL staining. Major organs were harvested for H&E staining. Tumor volume = 1/2 × width^2 × length. The function of the major organs of control group and OLA-NDs group was evaluated after 30 days. The main serological indicators included hepatic function—alanine aminotransferase (ALT), aspartate aminotransferase (AST), and albumin (ALB), kidney function—blood urea nitrogen (BUN), creatinine (CREA), and uric acid (UA), and cardiac function—creatine kinase (CK) and creatine kinase isoenzyme (CK-MB).

2.17. Statistical analysis

All data were displayed as mean±SD. One-way ANOVA was applied for multiple groups. Student's t-test was applied for two groups. *p < 0.05, **p < 0.01, ***p < 0.001 and ****p < 0.0001 was shown to be statistically significant.

3. Results and discussion

3.1. Preparation and characterization of OLA-NDs

The synthetic procedure of OLA-NDs was shown in Fig. 2A. OLA-NDs were first prepared by a homogeneous emulsion method, OLA was successfully loaded into OLA-NDs. TEM was used to investigate the morphology of NDs in different pH. OLA-NDs were well-dispersed with a spherical shape at pH 7.4 (pH of blood circulation) (Fig. 2B). As shown in Fig. 2C, OLA-NDs displayed acid-responsive swelling and aggregation at pH 5.5 (pH of endosomes). Tumor dependence on aerobic glycolysis, which makes the TME acidic, pH difference between normal and tumor tissue could be exploited to increase drug concentrations at the lesion site [33,34]. O-CMC could regulate its own solubility and surface charge conversion in response to pH changes, thus O-CMC-based nanocarriers could accumulate and release drugs in acidic TME [35]. To further examine the pH response of OLA-NDs, DLS was applied to determine their size and potential at different pH environments. OLA-ND has a particle size of 266.0 nm with PDI of 0.163 at pH 7.4, (Fig. 2D). As shown in the particle size distribution (Fig. 2E), OLA-NDs were stable at both pH 7.4 and pH 6.5 (pH of TME), whereas the particle size and PDI of OLA-NDs increased dramatically at pH 5.5, suggesting that OLA-NDs was expanded and aggregated at pH 5.5. ζ potential change of OLA-NDs under different pH confirmed its acid-responsive charge conversion ability (Fig. 2F). At pH 7.4, the ζ potential of OLA-NDs was negative (−6.15 ± 1.0 mV), suggesting that it could be applicable for DDSs as the negative charge could prevent them from being removed prematurely in circulation. The ζ potential of OLA-NDs was converted to a positive value at pH 6.5, thus promoting accumulation and cell internalization in tumors [36]. Besides, we also found that the ζ potential was close to zero at pH 6.8 (Fig. S1). Compared with freshly prepared NDs, its particle size and PDI showed less variation in the simulated blood environment and lyophilized state, which indicated satisfactory stability (Fig. S2).

When the OLA dosage was 1.5 mg, OLA-NDs exhibited optimal EE and LE, 50.3 % and 12.6 % respectively (Fig. S3A). And there was no statistically significant difference in EE between fresh and lyophilized nanodrops (Fig. S3B). Optimal tumor-targeted DDSs should release drugs in rapid response to TME after accumulation in tumor. The behavior of drug release from OLA-NDs at different pH and US exposure was evaluated. OLA release from OLA-NDs was relatively slow at pH 7.4, suggesting that OLA-NDs were able to preserve the drug effectively in the blood circulation with less leakage. In contrast, at pH 6.5 and pH 5.5, OLA-NDs released OLA rapidly and sustainably over 24 h, with cumulative releases of 51.7 ± 3.3 % and 75.8 ± 2.8 %, respectively (Fig. 2G). After US irradiation, OLA-NDs exhibited instantaneous release, with up to 72.1 ± 2.5 % release within 8 min (Fig. 2H). Meanwhile, a negligible amount of drug was released from OLA-NDs with the absence of US stimulation. TME has a special physicochemical environment, resulting in a complex metabolic pattern [37]. Single-response DDSs respond slowly at the tumor site, which prevents the drug from being fully released, leading to mediocre therapeutic effects [38]. Under different pH conditions, the drug release increased accordingly with decreasing pH, and the cumulative releases after 2 min of US stimulation were 34.5 ± 2.6 %, 43.6 ± 1.2 %, and 53.1 ± 5.0 % ($P < 0.05$), respectively (Fig. S4). The above results strongly supported that OLA-NDs could release drugs via both endogenous pH response and exogenous US stimulation, which is expected to serve as effective anti-tumor DDSs.

3.2. Biocompatibility and echogenicity of NDs

The prerequisite for DDSs applications is good biocompatibility. As shown in Fig. 3A, even with NDs concentrations as high as 600 μg/mL, the hemolysis rate was less than 5 %. In addition, NDs ranging from 20 to 600 μg/mL had a negligible effect on cell viability (Fig. 3B), suggesting that NDs have the advantages of low toxicity and hemocompatibility as DDSs. Perfluorocarbon liquids can undergo a phase transition upon exposure to sufficiently powerful US and a temperature increase, and the resulting microbubbles can be used for imaging or therapeutic delivery [39,40]. Next, we explored the responsiveness of NDs with a PFH core to temperature and US irradiation. We found the size of NDs increased significantly when exposed to US due to the ADV of PFH (Fig. S5). In addition, we examined the particle size of NDs under US exposure by DLS which showed that the ND particle size increased to 835 nm (Fig. S6). However, no significant changes in NDs were observed at 25 °C and 37 °C (Fig. S7), indicating that NDs were stabilized at both temperatures, which ensured that they did not experience phase transition in circulation before reaching the targeting site. To further evaluate the echogenicity of NDs, *in vitro* and *in vivo* US imaging was acquired using CEUS mode. After US irradiation, OLA-NDs exhibited a strong echo signal at CEUS mode *in vitro*. In contrast, no significant echo signal was observed with PBS (Fig. 3C). As shown in Fig. 3D, after PBS was administered intravenously to mice, the tumor was the same as before injection, with almost no echo signal. In contrast, when the tumor area in the OLA-NDs group experienced US irradiation, the echo signal increased significantly and almost filled the entire tumor. Taken together, OLA-NDs exhibited good biocompatibility and enhanced contrast imaging for real-time US imaging guidance.

3.3. Intracellular uptake and tumor-targeting efficiency of NDs

CLSM was employed to assess the cellular internalization of Dil-labeled NDs. Red fluorescence representing NDs was observed intracellularly at pH 7.4, and the fluorescent intensity increased significantly when the surrounding environment was pH 6.5 (Fig. 4A), implying that the charge of NDs on the O-CMC surface was inverted to be positive at pH 6.5, which facilitated the interaction of NDs with the negatively charged cell membrane. Since the pH of the tumor microenvironment is different from that of normal tissues, we observed the uptake of NDs in A2780 cells (human ovarian cancer cell) and LX2 cells (human hepatic stellate cell). As shown in Fig. S8, NDs uptake by A2780 cells was significantly more compared to LX2 cells, indicating that NDs would be able to target the tumor site. UTMD could increase cell membrane permeability through sonoporation to promote cell internalization [41]. A significant accumulation of red fluorescence was observed around the nucleus after US irradiation (Fig. 4B), suggesting that in addition to surface charge reversal, NDs could be internalized by cells through UTMD-mediated sonoporation.

In vivo, tumor targeting of NDs was examined with IVIS using A2780 tumor-bearing mice as a model (Fig. 4C). As shown in Fig. 4D, after administration via the tail vein, the accumulation of fluorescent signal of NDs in the tumor increased and then decreased, reaching a peak at 4 h. Fluorescent signals that accumulated in the tumor were still visible after 24 h, indicating the long retention and enhanced permeability and

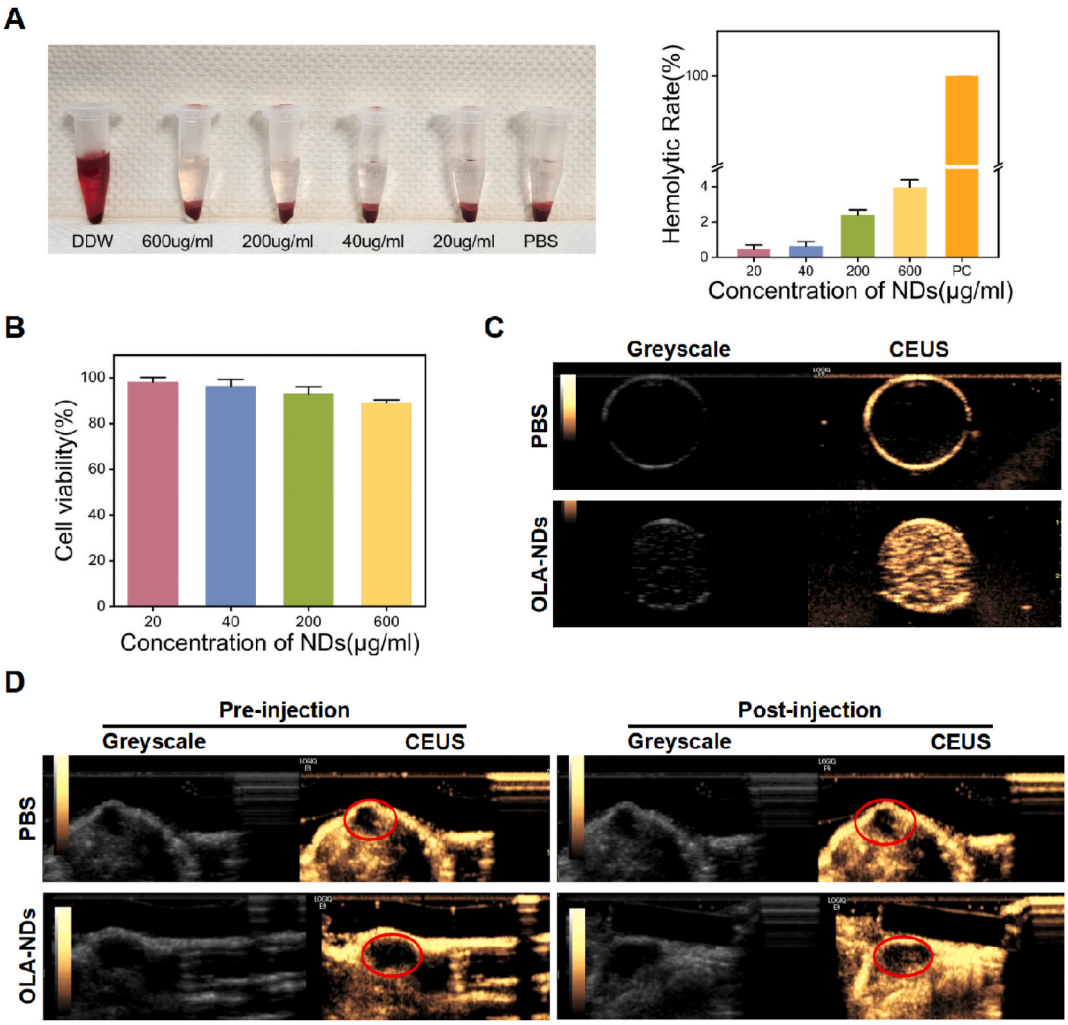

Fig. 3. Biocompatibility and Echogenicity of NDs (A) Hemolysis assay with NDs at different concentrations (B) Cell viability of NDs with different concentrations. (C) US imaging of OLA-NDs. (D) US imaging of OLA-NDs in tumor-bearing mice. Red circle indicates tumor site. (For interpretation of the references to colour in this figure legend, the reader is referred to the Web version of this article.)

retention effects of NDs. At this point, mice were executed to isolate tumors and major organs for imaging and quantification of the biodistribution of NDs. As shown in Fig. 4E and F, a certain percentage of fluorescent signals were observed in the liver and kidney, which may result from the fact that part of the NDs were phagocytosed by the hepatic reticuloendothelial system during systemic circulation, and then metabolized and eliminated from the body by the kidney. Frozen sections of tumor tissues showed significant intracellular red fluorescence around the nuclei (Fig. 4G), which further indicated that NDs possessed the ability to penetrate and target A2780 tumors.

3.4. *UTMD combined with OLA-NDs induces DNA oxidative damage*

To assess the state of oxidative stress by measuring intracellular ROS, DCFH-DA was employed as an indicator and oxidized to emit green fluorescence. US-irradiated A2780 cells produced a large amount of ROS, with the strongest green fluorescence in the OLA-NDs + US group (Fig. 5A). Notably, OLA and OLA-NDs also produced a certain amount of ROS, which was attributed to the fact that PARPi also increase oxidative stress in addition to compromising DNA repair [42]. This result indicated that UTMD combined with OLA-NDs could amplify oxidative stress.

In preliminary experiments (Fig. S9), we evaluated the sensitivity of BRCA wild-type ovarian cancer cell lines (SKOV3 and A2780) to OLA and observed that A2780 cells were less drug-sensitive than SKOV3 cells. Therefore, we chose A2780 cells as a model to validate the efficacy. It has been reported that overproduction of ROS would trigger DNA damage, we investigated whether UTMD combined with OLA-NDs induces DNA damage in A2780 cells. The alkaline comet assay detects DNA strand breaks in a tail-rectangular manner, reflecting the extent of DNA damage (Fig. 5B). A significant increase in the TailDNA% was seen in OLA-NDs + US group, suggesting serious DNA damage occurred in cells. Quantitative results displayed that OLA-NDs + US group showed significantly higher DNA damage than the other groups (Fig. 5C), which might be related to the PARP activity inhibited by OLA. PARP family proteins, especially PARP1 and PARP2, are catalytic enzymes that rapidly respond to DNA damage and initiate DNA repair [43]. As shown in Fig. 5D, PARP-1 and PARP-2 activities were significantly increased in NDs + US group compared to control group, while PARP activities were decreased in OLA-NDs + US group compared to ND + US group. The phenomenon suggested that UTMD can lead to severe DNA damage, whereas OLA was released to inhibit PARP activity, consequently leading to the accumulation of SSB in cells within the combined treatment group due to impaired repair mechanisms. To confirm that UTMD combined with OLA-NDs produced DSBs in A2780 cells, we next examined γ-H2AX, a biomarker for DNA DSBs (Fig. 5E). The result showed that the mean fluorescence intensity (MFI) of the OLA-NDs + US group was 3.19 times of the control group and 2.04 times of the OLA

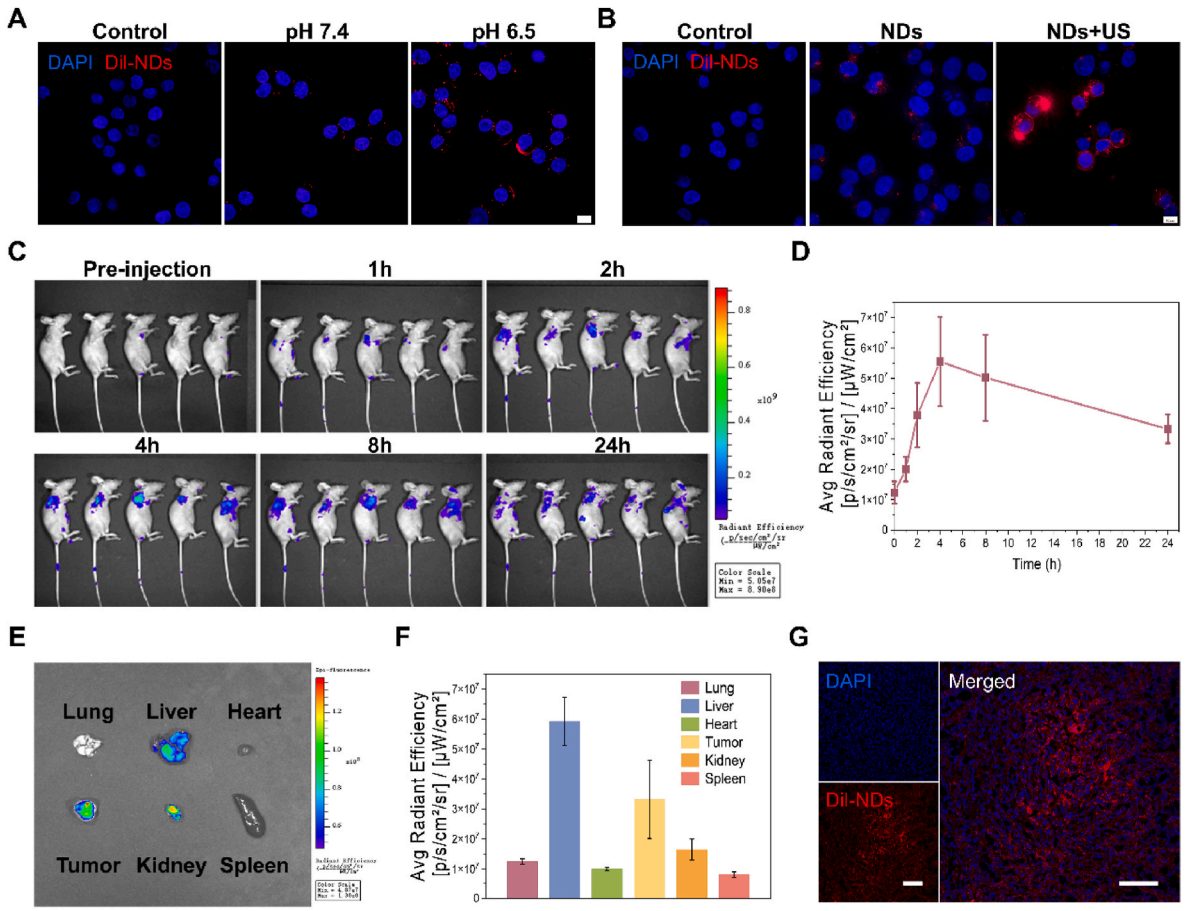

Fig. 4. Intracellular uptake and tumor-targeting efficiency. (A) Intracellular uptake of Dil-NDs by A2780 cells at different pH. Scale bar: 10 μm. (B) Intracellular uptake of Dil-NDs by A2780 cells under US irradiation. Scale bar: 10 μm (C) Tumor-bearing mice were imaged after injection. (D) Quantification of the average signal at tumor region. (E) Biodistribution of the NDs after 24 h. (F) Quantification of the average signal. (G) Images of NDs accumulation in tumor. Scale bar: 100 μm.

group (Fig. S10), supporting increased DNA DSBs formation. In addition, cell cycle experiments showed that UTMD combined with OLA-NDs induced more S-phase accumulation (Fig. S11), suggesting that the combined therapy resulted in a failure of the cell cycle to proceed smoothly and blocked DNA synthesis [44].

To determine that the DNA damage caused by the combination therapy resulted from ROS, we treated A2780 cells with NAC (ROS scavenger) and observed that both DNA strand breaks and γ-H2AX accumulation were reversed in the OLA-NDs + US group by the addition of NAC (Fig.S12 and Fig.S13). In addition, 8-OHdG, a marker of oxidative DNA damage, accumulated more on A2780 cells in OLA-NDs + US group compared to the other groups (Fig. 5F and Fig. S14). These results suggested that oxidative DNA damage resulting from combination therapy-mediated ROS overproduction was associated with DNA DSBs formation.

Based on the above, it could be concluded that UTMD combined with OLA-NDs could lead to increased DNA damage in BRCA wild-type A2780 cells by generating ROS causing oxidative stress and blocking DNA repair pathways.

3.5. *UTMD combined with OLA-NDs amplifies oxidative stress by interrupting mitochondrial function*

NOX4 is the major source of cellular ROS, and its overactivation would lead to increased oxidative stress [45,46]. To investigate whether NOX4 plays a role in amplifying oxidative stress during combination therapy, we analyzed cellular NOX4 protein levels in each group. As shown in Fig. 6A, after US irradiation, A2780 cells exhibited an enhanced red fluorescence, implying that UTMD upregulated NOX4 expression. Besides, the highest NOX4 expression was observed in OLA-NDs + US group (Fig. S15), which is in agreement with the results of ROS generation, suggesting NOX4 is a target for UTMD to amplify oxidative stress by binding to OLA-NDs. In addition, compared with OLA-NDs + US group without NOX-4 inhibitor (GLX351322), the fluorescence intensity of ROS in cells pretreated with NOX-4 inhibitor was obviously weakened, suggesting that ROS generated by the combination of OLA-NDs with UTMD were mainly from NOX-4 (Fig. S16).

NOX4-produced ROS not only contributes to oxidative stress but also to mitochondrial dysfunction and cell death. We next investigated the effect of combination therapy on mitochondria. JC-1 staining was first used to examine the combination therapy-induced MMP changes. In normal mitochondria, JC-1 shows polymers that emit red fluorescence, whereas JC-1 shows monomers that emit green fluorescence in damaged mitochondria due to the reduction of MMP. As shown in Fig. 6B, OLA-NDs + US group exhibited an increased JC-1 monomer/polymer ratio compared to OLA-NDs group or NDs + US group, indicating combination therapy induces MMP loss and mitochondrial damage. We further performed TEM to observe the mitochondrial structure of A2780 cells subjected to different treatments. The number of normal mitochondria was decreased in the other groups compared to control and NDs groups. Especially, OLA-NDs + US group displayed swollen mitochondria, mitochondrial cristae breakdown, and vacuolization in the matrix, suggesting that the combination of UTMD with OLA-NDs severely damaged the mitochondrial structure (Fig. 6C). Given that mitochondrial dysfunction also generates ROS [47], UTMD combined with OLA-NDs could amplify oxidative stress by interrupting mitochondrial

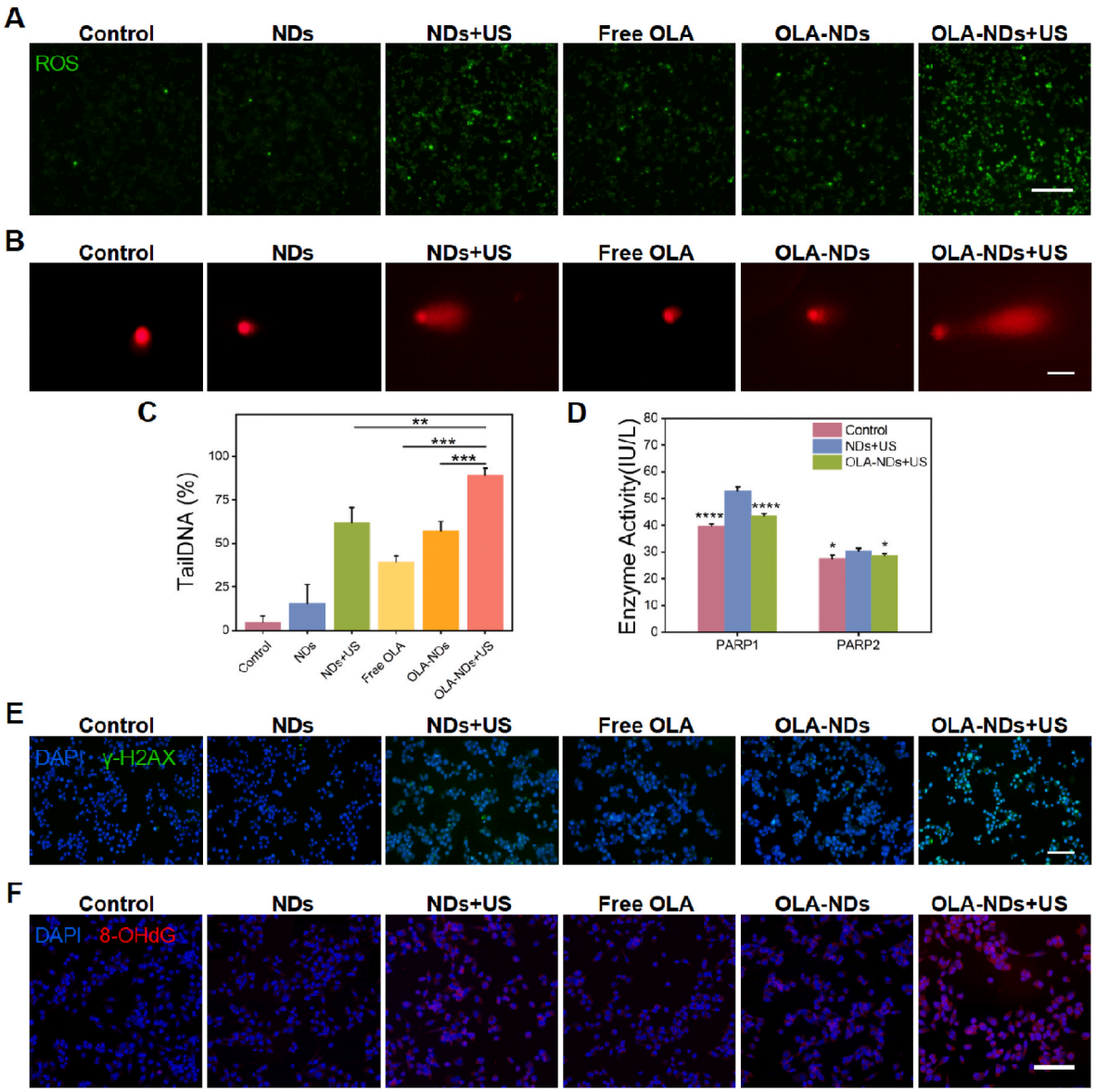

Fig. 5. UTMD combined with OLA-NDs amplifies DNA oxidative damage. (A) Images of ROS generation in A2780 cells. Scale bar: 100 μm. (B) Images of comet assay of in A2780 cells. Scale bar: 50 μm. (C) Quantification of tail moments with different treatments. (D) Analysis of PARP activity. (E) Immunofluorescence image for γ-H2AX on A2780 cells. Scale bar: 100 μm. (F) Image of 8-OHdG on A2780 cells. Scale bar: 100 μm.

function.

Mitochondria are regulatory centers for apoptosis responses to therapy-induced stress signals in cancer cells [48,49]. To further verify mitochondria-mediated apoptosis, we investigated the effect of combined therapy on the expression of mitochondrial apoptosis coregulators BAX and Bcl-2. BAX is a pro-apoptotic protein that is located in the outer mitochondrial membrane. On the contrary, Bcl-2 inhibits BAX activity to prevent alteration of mitochondrial membrane permeability and apoptosis [50]. When detecting the expression of BAX and Bcl-2, it was found that in the OLA-NDs + US group, the expression of BAX was upregulated and the expression of Bcl-2 was downregulated (Fig. 6D). This change suggests that the mitochondrial-mediated apoptotic pathway was significantly activated. Quantitative analysis of protein expression also confirmed this statement (Fig. S17). Overall, it can be seen that combination therapy upregulates NOX4-produced ROS, leading to mitochondrial dysfunction and secondary ROS production, which together with NOX4-produced ROS could result in the accumulation of additional ROS, creating a cycle of oxidative stress that promotes apoptosis.

3.6. *In vitro antitumor efficacy*

To examine the antitumor effect of the oxidative damage amplified therapy, the cytotoxicity of UTMD combined with OLA-NDs was investigated by Calcein AM/PI staining. The green fluorescent dots represent live cells and the red fluorescent dots represent dead cells. The highest red/green ratio was observed in OLA-NDs + US group, which indicated that combined therapy could lead to maximum cell death with the strongest inhibitory effect on cancer cells (Fig. 7A). EdU assay was used to determine the efficacy of the combination therapy on the proliferation of A2780 cells. The lowest percentage of EdU-positive cells was observed in the OLA-NDs + US group, indicating that this combination therapy significantly inhibited the proliferation of cancer cells (Fig. 7B and C). As shown in Fig. 7D, free OLA exhibited limited effects on the viability of A2780 cells. Notably, OLA-NDs + US group showed stronger cytotoxicity than OLA group, OLA-NDs + US group, and NDs + US group. Besides, we also performed a dose-response curve of OLA-NDs, and the result showed that IC50 was 38.77 μg/mL without US and 26.95 μg/mL with US (Fig. S18), indicating that the synergistic effect of UTMD and

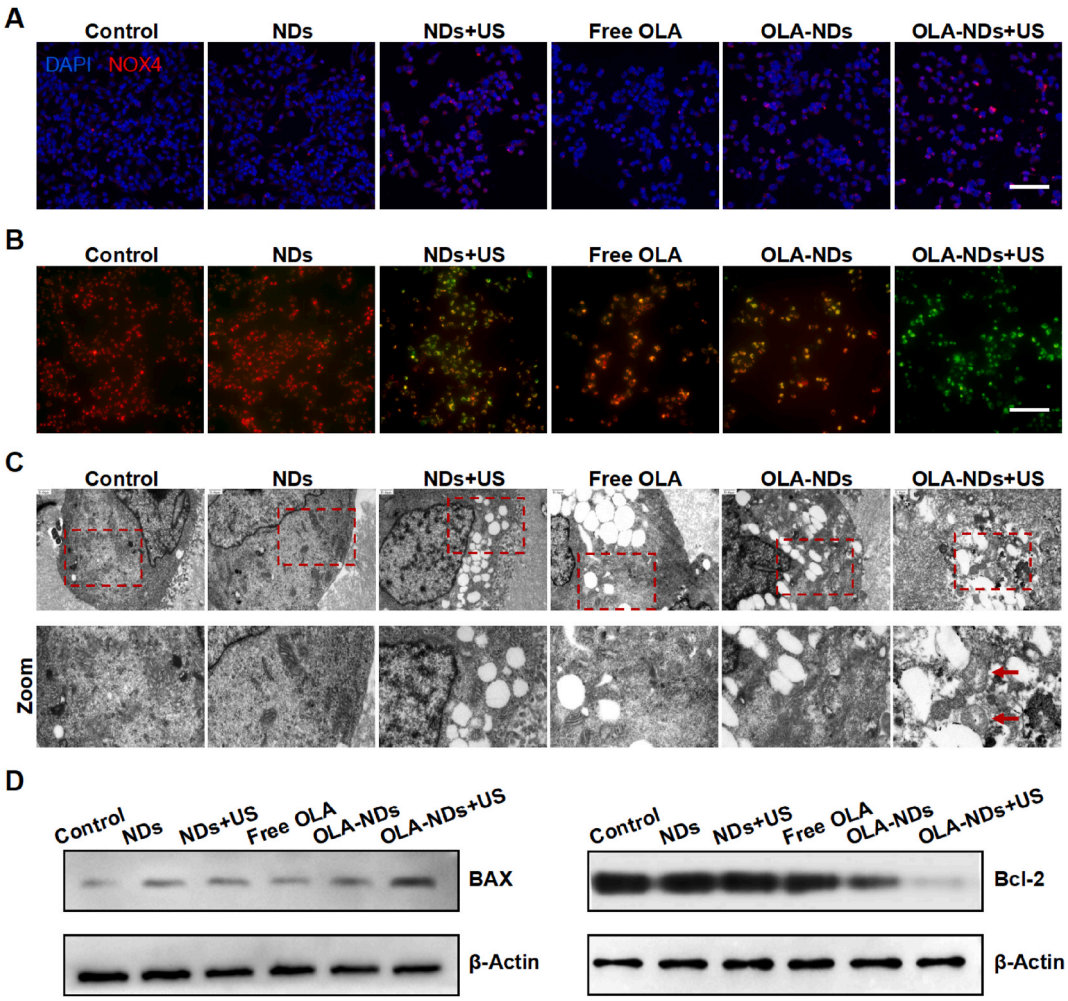

Fig. 6. UTMD combined with OLA-NDs disrupts mitochondrial function. (A) Immunofluorescence image for NOX4 on A2780 cells. Scale bar: 100 μm. (B) Images of JC-1-stained A2780 cells. Scale bar: 100 μm. (C) TEM image of A2780 cells. Scale bar: 0.6 μm. Red arrows indicate swollen mitochondria. (D) Expression of BAX and Bcl-2 on A2780 cells with different treatments. (For interpretation of the references to colour in this figure legend, the reader is referred to the Web version of this article.)

OLA-NDs enhanced cytotoxicity.

Next, wound healing assay and transwell assay were performed to assess the migration and invasion of A2780 cells. The relative rate of wound healing for the OLA-NDs + US group was 25.5 ± 7.7 %, with negligible change in scratches after 48 h. In contrast, the relative rates of wound healing in the NDs + US group and OLA-NDs group were 57.6 ± 6.1 % and 61.8 ± 4.8 %, respectively (Fig. 7E and G). The number of invading cells in the NDs + US group, free OLA group, and OLA-NDs group were 76 ± 18, 137 ± 13, and 95 ± 12, respectively, and the OLA-NDs + US group displayed the lowest number was 18 ± 9 (Fig. 7F and H), suggesting that the effectiveness of combined therapy in suppressing cell migration and invasion.

The above result suggests that the combined strategy of amplifying oxidative damage could effectively inhibit cancer cell proliferation, enhance cytotoxicity, and suppress their migration and invasion.

3.7. *In vivo* antitumor efficacy and preliminary safety evaluation

Given the significant antitumor efficacy of UTMD and OLA-ND *in vitro*, we investigated their antagonistic effects and mechanisms for xenografted tumors (Fig. 8A). Tumors were excised on day 12 (Fig. 8B). As shown in Fig. 8C, it might be due to the biocompatibility of NDs, mice treated with NDs displayed similar rates of tumor growth compared to control group. Besides, the OLA group and the NDs + US group displayed moderate retardation of tumor growth, indicating that monotherapy was insufficient to control tumor progression. Compared with the other groups, tumor growth could be inhibited more effectively under the combined treatment of UTMD and OLA-NDs. The tumor weight in the OLA-NDs + US group (0.46 ± 0.19 g) was 2.30-fold less than that in the OLA-NDs group (1.06 ± 0.16 g) and 2.28-fold less than that in the NDs + US group (1.05 ± 0.21 g), which is strong evidence for the effectiveness of the combination of UTMDs combined with OLA-NDs in inhibiting tumor growth (Fig. 8D). H&E staining of the tumors displayed that the OLA-NDs + US group presented the maximum area of severely damaged (nuclear atrophy and fragmentation) tumor cells. Moreover, similar results have also been observed in the TUNEL assay with red fluorescence representing apoptosis cells. The IHC staining of Ki67 results revealed that the proliferation of tumor cells in the OLA-NDs + US group was markedly decreased (Fig. 8F). The above results revealed a cumulative antitumor effect between OLA-NDs and UTMD, this may be a synergistic effect of oxidative stress-enhanced DNA damage and blocked DNA repair.

Subsequently, we determined the antitumor mechanism of the combined therapy *in vivo*. As shown in Fig. 8G, UTMD combined with OLA-NDs was shown to be effective in increasing the expression of γ-H2AX and 8-OHdG, which implied that DNA was severely damaged. Moreover, compared with the control group and NDs group, the expression of BAX was increased in each group, whereas the expression

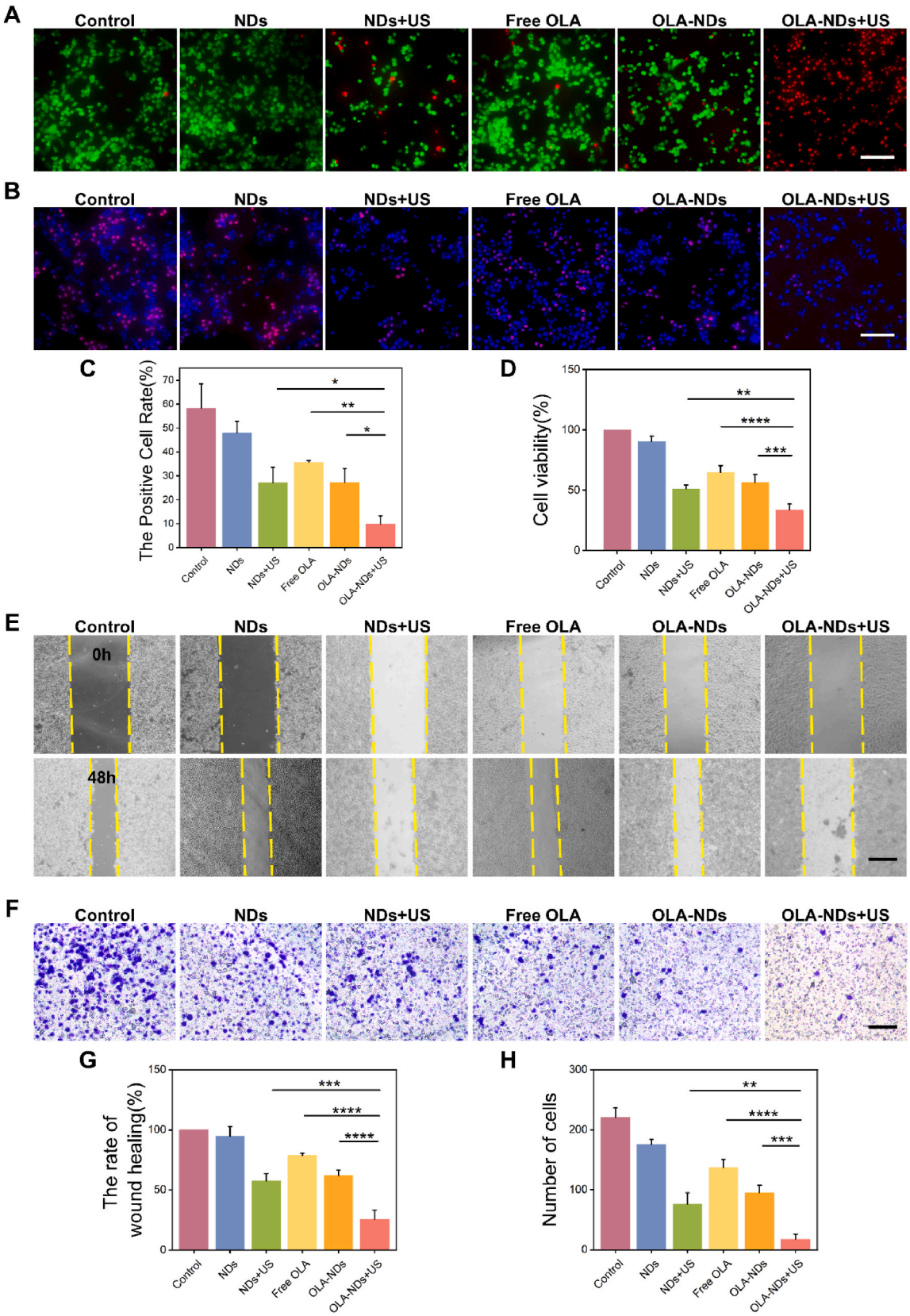

Fig. 7. In vitro antitumor efficacy. (A) Images of A2780 cells stained with Calcein AM and PI. Scale bar: 100 μm. (B) Images of EdU-positive cells from different groups. Scale bar: 100 μm. (C) Quantification of EdU-positive cell rate. (D) Cell viability of A2780 cells from different groups. (E) Wound healing assay of A2780 cells from different groups. Scale bar: 200 μm. (F) Transwell invasion assays of A2780 cells in different groups. Scale bar: 100 μm. (G) Quantify the area of migration. (H) Number of invading cells.

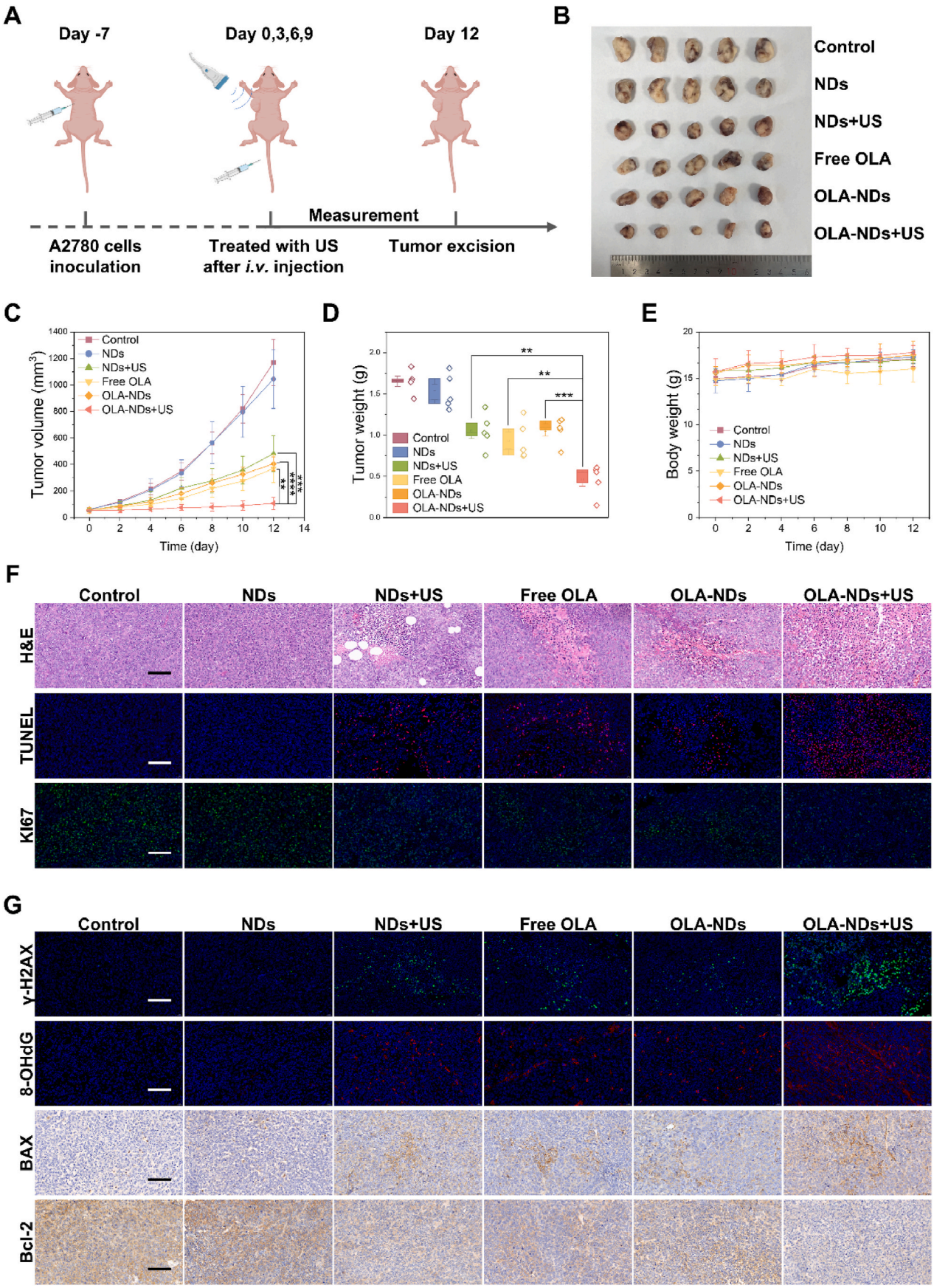

Fig. 8. In vivo antitumor efficiency. (A) Illustration of the treatment of xenografted tumors. (B) Photograph of isolated tumors. (C) Tumor growth curves. (D) Weight of tumors in different groups. (E) Changes in body weight of mice. (F) Images of H&E, TUNEL and Ki67 staining from different groups. Scale bar: 100 μm. (G) Images of γ-H2AX, 8-OHdG, BAX and Bcl-2 immunostaining from different groups. scale bar: 100 μm.

of Bcl-2 was significantly decreased. The results indicated that the antitumor effect of the combined therapy *in vivo* was associated with enhanced DNA damage and mitochondria-mediated apoptosis.

After treatment with different formulations, a slight increase in body weight could be monitored in all groups of mice, and no significant adverse effects were observed (Fig. 8E). No apparent pathological changes were found on major organs in all groups of mice (Fig. S19). Furthermore, to evaluate major organ function after long-term drug administration, we injected OLA-NDs into mice and examined serological indicators after 30 days (Fig. S20), which showed no myocardial injury and no changes in hepatic or kidney function ($P>0.05$), further indicating that all the formulations have excellent biosafety for living animals. These results indicated the combination of UTMD and OLA-NDs can potently suppress tumor growth without significant systemic toxicity.

4. Conclusion

In summary, we fabricated OLA-NDs to enhance oxidative damage for tumor inhibition with the utilization of UTMD. UTMD combined with OLA-NDs exhibited improved cell internalization behavior and tumor-target drug delivery. UTMD could cause oxidative DNA damage in A2780 cells by upregulating NOX4-produced ROS, leading to DNA DSBs. Moreover, this combination therapy further increased ROS production by interfering with mitochondrial function, which exacerbated the DNA damage in conjunction with DNA repair blockade, thereby synergistically killing A2780 cells and inhibiting the growth of A2780 tumors. The current findings offer exciting possibilities for expanding PARPi in BRCA-proficient ovarian cancer. This study also has limitations such as the lack of comparative validation of different types of ovarian cancer cells (e.g., BRCA-deficient and BRCA-proficient) and mouse models.

CRediT authorship contribution statement

Jialu Zhang: Project administration, Methodology, Investigation, Formal analysis, Data curation. **Xiaoxuan Wang:** Writing – review & editing, Writing – original draft, Visualization, Validation. **Lu Guo:** Formal analysis. **Shan Xiao:** Conceptualization. **Dong Meng:** Supervision. **Mengmeng Shang:** Data curation. **Xiao Sun:** Resources. **Dandan Shi:** Project administration. **Yading Zhao:** Methodology. **Rui Liu:** Project administration. **Shuting Huang:** Investigation. **Xinyu Zeng:** Software. **Jie Li:** Supervision, Project administration, Funding acquisition.

Ethics approval and consent to participate

Qilu Hospital of Shandong University's Laboratory Animal Ethics Committee authorized the protocols for the animal experiments.

Declaration of competing interest

The authors declare that they have no known competing financial interests or personal relationships that could have appeared to influence the work reported in this paper.

Acknowledgement

This work was supported by Taishan Scholar Foundation of Shandong Province, National Natural Science Foundation of China (No. 82471992, 82071937).

Appendix A. Supplementary data

Supplementary data to this article can be found online at https://doi.org/10.1016/j.mtbio.2025.101761.

Data availability

Data will be made available on request.

References

[1] R.L. Siegel, K.D. Miller, H.E. Fuchs, A. Jemal, Cancer statistics, 2022, CA Cancer J. Clin. 72 (2022) 7–33.
[2] I. Saani, N. Raj, R. Sood, S. Ansari, H.A. Mandviwala, E. Sanchez, S. Boussios, Clinical challenges in the management of malignant ovarian germ cell tumours, Int. J. Environ. Res. Publ. Health 20 (12) (2023 Jun 9) 6089.
[3] A. Ghose, L. McCann, S. Makker, U. Mukherjee, S.V.N. Gullapalli, J. Erekkath, S. Shih, I. Mahajan, E. Sanchez, M. Uccello, M. Moschetta, S. Adeleke, S. Boussios, Diagnostic biomarkers in ovarian cancer: advances beyond CA125 and HE4, Ther. Adv. Med. Oncol. 16 (2024 Feb 29) 17588359241233225.
[4] L.A. Torre, B. Trabert, C.E. DeSantis, K.D. Miller, G. Samimi, C.D. Runowicz, et al., Ovarian cancer statistics, 2018, CA Cancer J. Clin. 68 (2018) 284–296.
[5] D.D. Bowtell, S. Böhm, A.A. Ahmed, P.-J. Aspuria, R.C. Bast, V. Beral, et al., Rethinking ovarian cancer II: reducing mortality from high-grade serous ovarian cancer, Nat. Rev. Cancer 15 (2015) 668–679.
[6] H. Fu, P. Liang, Q. Chen, Y. Wang, G. Li, X. Cai, et al., COX-2 blocking therapy in cisplatin chemosensitization of ovarian cancer: an allicin-based nanomedicine approach, Chin. Chem. Lett. 35 (2024) 109241.
[7] F. Aliyuda, M. Moschetta, A. Ghose, K. Sofia Rallis, M. Sheriff, E. Sanchez, E. Rassy, S. Boussios, Advances in ovarian cancer treatment beyond PARP inhibitors, Curr. Cancer Drug Targets 23 (6) (2023) 433–446.
[8] J. Nonnekens, M. van Kranenburg, C.E.M.T. Beerens, M. Suker, M. Doukas, C.H. J. van Eijck, et al., Potentiation of peptide receptor radionuclide therapy by the PARP inhibitor olaparib, Theranostics 6 (2016) 1821–1832.
[9] A. Sonnenblick, E. De Azambuja, H.A. Azim, M. Piccart, An update on PARP inhibitors - moving to the adjuvant setting, Nat. Rev. Clin. Oncol. 12 (2015) 27–41.
[10] A. Ghorai, T. Mahaddalkar, R. Thorat, S. Dutt, Sustained inhibition of PARP-1 activity delays glioblastoma recurrence by enhancing radiation-induced senescence, Cancer Lett. 490 (2020) 44–53.
[11] J. Ledermann, P. Harter, C. Gourley, M. Friedlander, I. Vergote, G. Rustin, et al., Olaparib maintenance therapy in patients with platinum-sensitive relapsed serous ovarian cancer: a preplanned retrospective analysis of outcomes by BRCA status in a randomised phase 2 trial, Lancet Oncol. 15 (2014) 852–861.
[12] H. Miao, H. Meng, Y. Zhang, T. Chen, L. Zhang, W. Cheng, FSP1 inhibition enhances olaparib sensitivity in BRCA-proficient ovarian cancer patients via a nonferroptosis mechanism, Cell Death Differ. 31 (2024) 497–510.
[13] J. Shen, W. Zhao, Z. Ju, L. Wang, Y. Peng, M. Labrie, et al., PARPi triggers the STING-dependent immune response and enhances the therapeutic efficacy of immune checkpoint blockade independent of BRCAness, Cancer Res. 79 (2) (2019 Jan 15) 311–319.
[14] A. González-Martín, B. Pothuri, I. Vergote, R. DePont Christensen, W. Graybill, M. R. Mirza, et al., Niraparib in patients with newly diagnosed advanced ovarian cancer, N. Engl. J. Med. 381 (25) (2019 Dec 19) 2391–2402.
[15] C.J. LaFargue, G.Z. Dal Molin, A.K. Sood, R.L. Coleman, Exploring and comparing adverse events between PARP inhibitors, Lancet Oncol. 20 (1) (2019) e15–e28.
[16] M.P. Dias, S.C. Moser, S. Ganesan, J. Jonkers, Understanding and overcoming resistance to PARP inhibitors in cancer therapy, Nat. Rev. Clin. Oncol. 18 (12) (2021) 773–791.
[17] Y. Liu, J. Zhou, Q. Li, L. Li, Y. Jia, F. Geng, et al., Tumor microenvironment remodeling-based penetration strategies to amplify nanodrug accessibility to tumor parenchyma, Adv. Drug Deliv. Rev. 172 (2021) 80–103.
[18] H. Xiao, X. Li, B. Li, Y. Zhong, J. Qin, Y. Wang, et al., Sono-promoted drug penetration and extracellular matrix modulation potentiate sonodynamic therapy of pancreatic ductal adenocarcinoma, Acta Biomater. 161 (2023) 265–274.
[19] C. Zhang, S. Chen, Q. Li, J. Wu, F. Qiu, Z. Chen, et al., Ultrasound-targeted microbubble destruction mediates gene transfection for beta-cell regeneration and glucose regulation, Small 17 (2021) 1–9.
[20] L. Fournier, T. de La Taille, C. Chauvierre, Microbubbles for human diagnosis and therapy, Biomaterials 294 (2023) 122025.
[21] X. Xiang, H. Pang, T. Ma, F. Du, L. Li, J. Huang, et al., Ultrasound targeted microbubble destruction combined with Fe-MOF based bio-/enzyme-mimics nanoparticles for treating of cancer, J. Nanobiotechnol. 19 (2021) 1–14.
[22] X. Wang, F. Li, J. Zhang, L. Guo, M. Shang, X. Sun, et al., A combination of PD-L1-targeted IL-15 mRNA nanotherapy and ultrasound-targeted microbubble destruction for tumor immunotherapy, J. Contr. Release 367 (2024) 45–60.
[23] Y. Zhao, D. Shi, L. Guo, M. Shang, X. Sun, D. Meng, et al., Ultrasound targeted microbubble destruction-triggered nitric oxide release via nanoscale ultrasound contrast agent for sensitizing chemoimmunotherapy, J. Nanobiotechnol. 21 (2023) 1–17.
[24] A. Kanakkanthara, X. Hou, T.L. Ekstrom, V. Zanfagnin, A.M. Huehls, R.L. Kelly, et al., Repurposing ceritinib induces DNA damage and enhances PARP inhibitor responses in high-grade serous ovarian carcinoma, Cancer Res. 82 (2022) 307–319.
[25] N. Pulliam, F. Fang, A.R. Ozes, J. Tang, A. Adewuyi, H. Keer, et al., An effective epigenetic-PARP inhibitor combination therapy for breast and ovarian cancers independent of BRCA mutations, Clin. Cancer Res. 24 (2018) 3163–3175.
[26] H. An, C. Yang, Z. Jiang, J. Yuan, Z. Qiu, L. Chen, et al., Luminescence-activated Pt (IV) prodrug for in situ triggerable cancer therapy, Chin. Chem. Lett. 35 (2024) 109134.

[27] Z. Mai, J. Zhong, J. Zhang, G. Chen, Y. Tang, W. Ma, et al., Carrier-free immunotherapeutic NanoBooster with dual synergistic effects based on glutaminase inhibition combined with photodynamic therapy, ACS Nano 17 (2023) 1583–1596.
[28] A. Vermot, I. Petit-Härtlein, S.M.E. Smith, F. Fieschi, NADPH oxidases (NOX): an overview from discovery, molecular mechanisms to physiology and pathology, Antioxidants 10 (6) (2021 Jun 1) 890.
[29] I. Szanto, NADPH oxidase 4 (NOX4) in cancer: linking redox signals to oncogenic metabolic adaptation, Int. J. Mol. Sci. 23 (5) (2022 Feb 28) 2702.
[30] P. Jangili, N. Kong, J.H. Kim, J. Zhou, H. Liu, X. Zhang, et al., DNA-Damage-Response-Targeting mitochondria-activated multifunctional prodrug strategy for self-defensive tumor therapy, Angew. Chem. 134 (2022).
[31] C.J. Lord, A. Ashworth, The DNA damage response and cancer therapy, Nature 481 (2012) 287–294.
[32] L. Schürmann, L. Schumacher, K. Roquette, A. Brozovic, G. Fritz, Inhibition of the DSB repair protein RAD51 potentiates the cytotoxic efficacy of doxorubicin via promoting apoptosis-related death pathways, Cancer Lett. 520 (2021) 361–373.
[33] V. Estrella, T. Chen, M. Lloyd, J. Wojtkowiak, H.H. Cornnell, A. Ibrahim-Hashim, et al., Acidity generated by the tumor microenvironment drives local invasion, Cancer Res. 73 (2013) 1524–1535.
[34] S. Huang, M. Shang, L. Guo, X. Sun, S. Xiao, D. Shi, et al., Hydralazine loaded nanodroplets combined with ultrasound-targeted microbubble destruction to induce pyroptosis for tumor treatment, J. Nanobiotechnol. 22 (2024) 1–13.
[35] S. Xiao, L. Guo, C. Ai, M. Shang, D. Shi, D. Meng, et al., PH-/Redox-Responsive nanodroplet combined with ultrasound-targeted microbubble destruction for the targeted treatment of drug-resistant triple negative breast cancer, ACS Appl. Mater. Interfaces (2022).
[36] Y. Dai, C. Xu, X. Sun, X. Chen, Nanoparticle design strategies for enhanced anticancer therapy by exploiting the tumour microenvironment, Chem. Soc. Rev. 46 (2017) 3830–3852.
[37] M.Z. Jin, W.L. Jin, The updated landscape of tumor microenvironment and drug repurposing, Signal Transduct. Targeted Ther. 5 (2020).
[38] J. Zhang, Y. Lin, Z. Lin, Q. Wei, J. Qian, R. Ruan, et al., Stimuli-responsive nanoparticles for controlled drug delivery in synergistic cancer immunotherapy, Adv. Sci. 9 (2022) 1–27.
[39] G. Wang, C. Zhang, Z. Huang, J. Chen, H. Chen, T. Lin, et al., Transcytosable and ultrasound-activated liposome enables deep penetration of biofilm for surgical site infection management, Adv. Mater. 2411092 (2024) 1–15.
[40] X. Wang, M. Shang, X. Sun, L. Guo, S. Xiao, D. Shi, et al., Dual-responsive nanodroplets combined with ultrasound-targeted microbubble destruction suppress tumor growth and metastasis via autophagy blockade, J. Contr. Release 343 (2022) 66–77.
[41] J.Y. Lee, D. Carugo, C. Crake, J. Owen, M. De Saint Victor, A. Seth, et al., Nanoparticle-loaded protein-polymer nanodroplets for improved stability and conversion efficiency in ultrasound imaging and drug delivery, Adv. Mater. 27 (2015) 5484–5492.
[42] D. Hou, Z. Liu, X. Xu, Q. Liu, X. Zhang, B. Kong, et al., Increased oxidative stress mediates the antitumor effect of PARP inhibition in ovarian cancer, Redox Biol. 17 (2018) 99–111.
[43] J.L. Riffell, C.J. Lord, A. Ashworth, Tankyrase-targeted therapeutics: expanding opportunities in the PARP family, Nat. Rev. Drug Discov. 11 (2012) 923–936.
[44] M. Andrs, H. Stoy, B. Boleslavska, N. Chappidi, R. Kanagaraj, Z. Nascakova, et al., Excessive reactive oxygen species induce transcription-dependent replication stress, Nat. Commun. 14 (2023) 1791.
[45] M.W. Park, H.W. Cha, J. Kim, J.H. Kim, H. Yang, S. Yoon, et al., NOX4 promotes ferroptosis of astrocytes by oxidative stress-induced lipid peroxidation via the impairment of mitochondrial metabolism in Alzheimer's diseases, Redox Biol. 41 (2021) 101947.
[46] B.-Y. Ding, C.-N. Xie, J.-Y. Xie, Z.-W. Gao, X.-W. Fei, E.-H. Hong, et al., Knockdown of NADPH oxidase 4 reduces mitochondrial oxidative stress and neuronal pyroptosis following intracerebral hemorrhage, Neural. Regen. Res. 18 (2022) 1734–17420.
[47] J. Wan, X. Zhang, Z. Li, F. Mo, D. Tang, H. Xiao, et al., Oxidative stress amplifiers as immunogenic cell death nanoinducers disrupting mitochondrial redox homeostasis for cancer immunotherapy, Adv. Healthcare Mater. 2202710 (2022) 1–15.
[48] K. Borankova, M. Krchniakova, L.Y.W. Leck, A. Kubistova, J. Neradil, P.J. Jansson, et al., Mitoribosomal synthetic lethality overcomes multidrug resistance in MYC-driven neuroblastoma, Cell Death Dis. 14 (2023).
[49] Y. Yang, Z. Mai, Y. Zhang, Z. Yu, W. Li, Y. Zhang, et al., A cascade targeted and mitochondrion-dysfunctional nanomedicine capable of overcoming drug resistance in hepatocellular carcinoma, ACS Nano 17 (2023) 1275–1286.
[50] A.Z. Spitz, E. Gavathiotis, Physiological and pharmacological modulation of BAX, Trends Pharmacol. Sci. 43 (2022) 206–220.